Quantum transport properties in single crystals of α-Bi_4I_4

Dong-Yun Chen,[1] Da-Shuai Ma,[1] Yongkai Li,[1] Z. Z. Du,[2,3,4] Xiaolu Xiong,[1,5] Yuan He,[1] JunXi Duan,[1] Junfeng Han,[1,5,*] Dong Chen,[6,†] Wende Xiao,[1,‡] and Yugui Yao[1]

[1]*Beijing Institute of Technology, Beijing Key Laboratory of Nanophotonics and Ultrafine Optoelectronic Systems, School of Physics, Beijing 100081, China*

[2]*Institute for Quantum Science and Engineering and Department of Physics, South University of Science and Technology of China, Shenzhen 518055, China*

[3]*School of Physics, Southeast University, Nanjing 211189, China*

[4]*Shenzhen Key Laboratory of Quantum Science and Engineering, Shenzhen 518055, China*

[5]*Micronano Center, Beijing Institute of Technology, Beijing 100081, China*

[6]*College of Physics, Qingdao University, Qingdao 266071, China*

(Received 17 May 2018; published 27 November 2018)

We report the magnetotransport properties of α-Bi_4I_4 single crystals, which have a crystal structure similar to that of the quasi-one-dimensional topological insulator β-Bi_4I_4. Prominent Shubnikov–de Hass oscillations and weak antilocalization effect are observed in all measured samples. The angular-dependent magnetoresistance indicates that the behavior of Shubnikov–de Hass oscillations is two-dimensional (2D) in n-type samples, while it is three-dimensional (3D) in p-type samples. First-principles calculations show that the n-type samples have a 2D Fermi surface, while the p-type samples have a 3D Fermi surface. Considering the similar carrier density and mobility, we infer that the transport behaviors in both types of samples come from bulk electron contributions. In addition, a large negative magnetoresistance with a transverse configuration is observed in the n-type sample A1. All the results indicate that α-Bi_4I_4 is an important material platform for investigation of novel and interesting phenomena. Our work may also provide important references for studying the topological surface transport properties in β-Bi_4I_4 in the future.

DOI: 10.1103/PhysRevMaterials.2.114408

I. INTRODUCTION

Topological insulators (TIs) are a new class of quantum materials characterized by an insulating energy gap in the bulk and gapless surface state [1–3]. The metallic surface state is protected by time-reversal symmetry and shows promising applications in spintronics and quantum computation. Potential applications of TIs are closely linked to the successful detection of transport properties on topological surface states (TSSs) [4], and Shubnikov–de Haas (SdH) oscillations have played important roles in studies of three-dimensional (3D) TIs [5–10]. At present, studies on the transport of TSSs rely largely on observations of two-dimensional (2D) transport characteristics, such as 2D SdH oscillations and the 2D weak antilocalization (WAL) effect [4–8]. However, topological trivial 2D electronic systems with these phenomena may confuse the identification of TSSs [10–13]. In addition, most of the existing 3D TIs are not perfect insulators in the bulk, and consequently bulk conduction may interfere with surface transport, which may affect the judgment of TSSs [9,10,14,15]. Exploring materials with transport properties similar to those of TIs will be helpful for identifying TSS transport in TIs.

Recently, Bi_4X_4 (X = Br, I) has been theoretically predicted to be a new family of TIs. Therein, β-Bi_4X_4's are regarded as 3D TIs and single-layer Bi_4Br_4 is a quantum spin Hall insulator [16–19]. On the other hand, while bulk α-Bi_4Br_4 is predicted as a high-order insulator with the emergence of the hinge state [20], bulk α-Bi_4I_4 is a trivial insulator [19]. Both α- and β-Bi_4X_4 have been experimentally confirmed or theoretically predicted to crystallize in quasi-one-dimensional crystal structures, which are piled up by identical 1D infinite chains of molecules in different interchain stacking patterns [19,21,22]. Angle-resolved photoemission spectroscopy studies have revealed a highly anisotropic band-crossing feature at the $\overline{M}$ point of the surface Brillouin zone in β-Bi_4I_4, verifying the strong TI phase [18]. On the other hand, α-Bi_4I_4, with a crystal structure similar to that of β-Bi_4I_4 [Fig. 1(a)], has scarcely been studied except in earlier synthetic and thermal stability experiments [21].

In this paper, we report the synthesis and magnetotransport properties of α-Bi_4I_4 single crystals. Most of the obtained crystals exhibit hole-carrier-dominated electrical transport (p type), and a small number of crystals are dominated by electron-type carriers (n type), which may embody the different Fermi level positions. In all measured samples, we observe the WAL effect in lower magnetic fields and SdH oscillations in higher fields. An obvious negative magnetoresistance (MR) component is observed in sample A1, with a magnetic field perpendicular to the current. For n-type samples, the SdH oscillations and WAL effect are 2D, while the SdH oscillations

*pkuhjf@bit.edu.cn
†dchen@qdu.edu.cn
‡wdxiao@bit.edu.cn

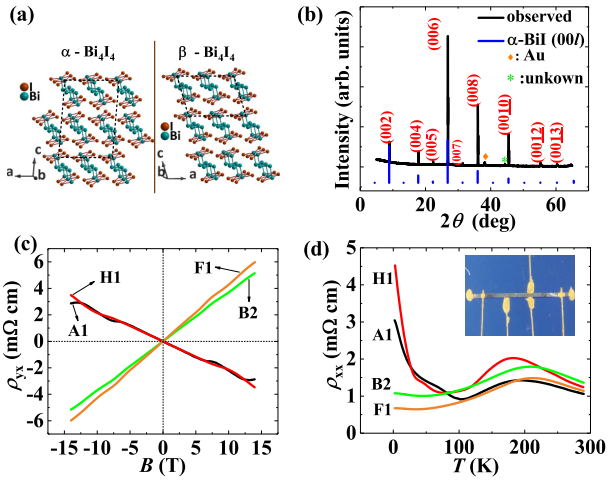

FIG. 1. (a) Crystal structure of quasi-one-dimensional α-Bi_4I_4 (left panel) and β-Bi_4I_4 (right panel). Bismuth and iodine atoms are shown in blue and brown, respectively. (b) XRD pattern of α-Bi_4I_4 single crystals with (00l) reflections, taken on a plane armed with gold electrodes for electrical transport measurements with the plane parallel to the substrate. The orange diamond indicates a Bragg peak from Au electrodes, and the green asterisk represents a minor and unspecified peak. (c) Magnetic-field dependence of the Hall resistivity ρ_{yx} at 2 K for samples A1, B2, H1, and F1, with the magnetic field perpendicular to the ab plane of the samples. (d) Temperature dependence of the electrical resistivity ρ_{xx} for the four samples. Inset: Image of a contacted sample for transport measurements.

in p-type samples are 3D. First-principles calculations reveal the 2D and 3D Fermi surfaces (FSs) in n-type and p-type samples, respectively, and give carrier densities consistent with the results of transport experiments. These results convince us that the transport behaviors of two types of samples originate from the bulk electrons. Additionally, a similar bulk electronic structure is found in β-Bi_4I_4, which makes α-Bi_4I_4 an important reference for future research on TSS transport in β-Bi_4I_4.

II. METHODS

Single crystals of α-Bi_4I_4 were grown using a chemical vapor transport method [18,22]. Bismuth metal powders and HgI_2 powders with a molar ratio of 2:1 were used as starting materials. A total mass of 2.5 g of the mixture was sealed in an evacuated quartz ampoule, which was then placed in a slightly tilted horizontal two-temperature-zone furnace. The starting materials were on the hot side, and the colder end of the ampoule was tilted upwards. The ampoule was heated and kept at a temperature gradient of 200°C/250°C for 2 weeks. After that, the furnace was slowly cooled down to room temperature. Needlelike crystals up to $10 \times 0.5 \times 0.2$ mm^3 in size were obtained near the cold zone of the ampoule.

The composition of the obtained single crystals was analyzed using energy-dispersive x-ray spectroscopy. The crystal structure was characterized by single-crystal x-ray diffraction (XRD) at room temperature using a Bruker single-crystal x-ray diffractometer with Mo-K_α radiation. A PAN-analytical x-ray diffractometer was also used to identify the crystal plane orientation with Cu-K_α radiation. Magnetotransport measurements were conducted using a physical property measurement system (Quantum Design) with a magnetic field up to 14 T and temperature down to 2 K. Strip-shaped crystals were attached with gold wires using gold paste for magnetotransport measurements. The five contacts were made such that current flows along the long axis (b axis) of the samples, and longitudinal and Hall voltages can be measured simultaneously [see inset in Fig. 1(d)]. The sample holder was mounted on a mechanical rotator with the spin axis aligned with the current. All the raw magnetotransport data were symmetrized or antisymmetrized in order to eliminate the misalignment effect of the contacts. The first-principles calculations were performed using the Vienna *ab initio* simulation package (VASP) [19]. The Perdew-Burke-Ernzerof generalized gradient approximation and the Heyd-Scuseria-Ernzerhof hybrid functional method (HSE06) were adopted as the exchange-correlation potential. Van der Waals–type corrections were used to optimize the ionic positions. To confirm the convergence of calculations, the kinetic cutoff energy was set at 300 eV, and a Γ-centered $6 \times 6 \times 3$ k-mesh was used to sample the Brillouin zone.

III. EXPERIMENTAL RESULTS

The atomic Bi:I ratio determined by energy-dispersive x-ray spectroscopy analysis is close to 1:1 (see Fig. S1 in the Supplemental Material [23]). Single-crystal x-ray diffraction confirms that all the single crystals used for electrical transport measurements are α-Bi_4I_4 with space group $C2/m$. The typical refined lattice parameters are $a = 14.213(7)$ Å, $b = 4.423(4)$ Å, $c = 19.939(7)$ Å, and $\beta = 92.91°$ (see Supplemental Table S1 for more information [23]), which are in accordance with previously reported values. In order to identify the top surface of samples, the XRD peaks were collected from 5° to 70°, as shown in Fig. 1(b). The main diffraction peaks can be indexed as the (00l) reflections of α-Bi_4I_4, suggesting that the measured plane is the ab plane. According to the standard data, the odd (00l) ($l = 2n + 1$) reflections are very weak and difficult to observe, which is consistent with our experimental observations. Considering that the ab-plane spacing of the α phase is close to twice that of the β phase, the observation of odd reflections (005) and (007) is further crucial evidence for identifying the phase as α-Bi_4I_4 rather than β-Bi_4I_4.

Magnetotransport measurements were performed on strip-shaped samples with the ab plane parallel to the top surface. The samples can be classified into two kinds according to the dominant carrier type: n type and p type. As shown in Fig. 1(c), the $\rho_{yx}(B)$ of A1 and H1 has a negative slope, corresponding to electron-dominant behavior (n type), and the positive slope for B2 and F1 corresponds to hole-dominant behavior (p type). This significant difference in the Hall measurements indicates that the two kinds of samples have different Fermi level positions in the band structure. The Hall resistivity $\rho_{yx}(B)$ of all four samples is nearly linear, superposed with magnetic oscillations. Figure 1(d) shows the temperature dependence of the longitudinal resistivity ρ_{xx} for the four pieces of single crystals. With decreasing temperature, the $\rho_{xx}(T)$ curves for all the samples roughly undergo

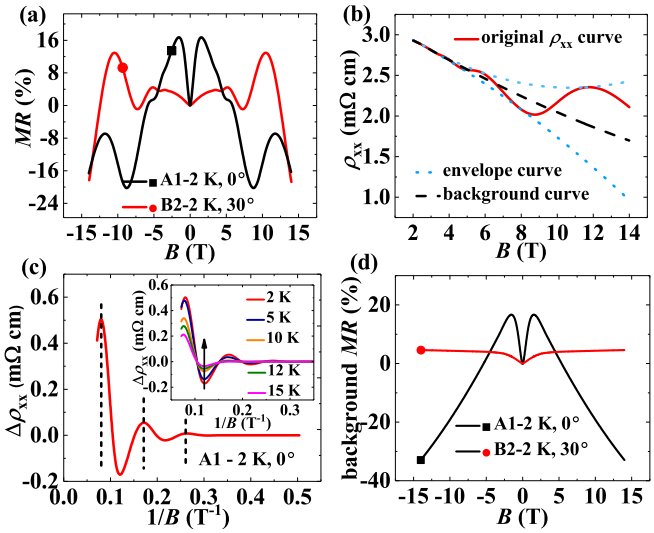

FIG. 2. (a) MR of samples A1 and B2 at 2 K measured at a magnetic field of from −14 to 14 T with $\theta = 0°$ and 30°, respectively [see the inset in Fig. 3(a)]. (b) Magnetic-field dependence of ρ_{xx} for sample A1 above 2 T at 2 K. Smooth envelope curves (short-dashed blue lines) are drawn by passing through the extremum points, and the average of the envelope curves is used to determine the background (dashed black lines). (c) Oscillatory component of the resistivity $\Delta\rho_{xx}$ in sample A1 plotted vs $1/B$ at 2 K and $\theta = 0°$, extracted by subtracting the smoothed background from ρ_{xx}. Inset: Oscillating resistivity $\Delta\rho_{xx}$ of A1 at different temperatures; the arrow represents the direction along which the temperature rises. (d) Overall background MR with a field of from −14 to 14 T at 2 K for A1 and B2 at $\theta = 0°$ and 30°, respectively.

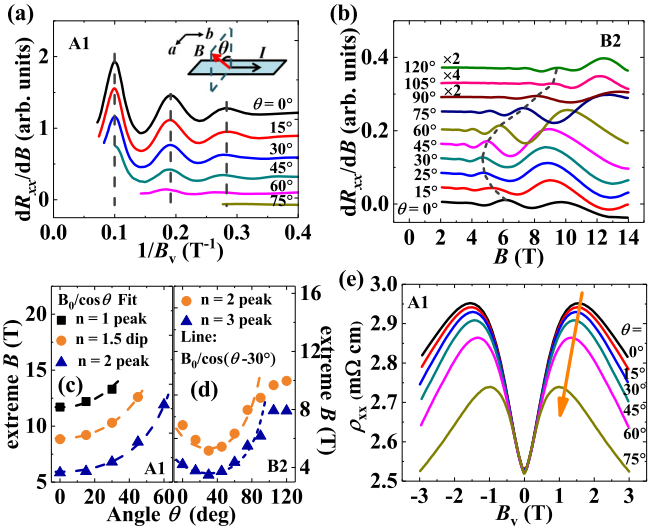

FIG. 3. (a) The resistance derivative dR_{xx}/dB versus $1/B_v = 1/(B\cos\theta)$ in sample A1 at varied tilt angles θ ($T = 2$ K). Dashed lines represent the positions of maxima. Inset: The measurement configuration, where θ is defined as the angle between the direction of the magnetic field and the normal direction of the sample substrate (//ab plane). (b) The resistance derivative dR_{xx}/dB versus B in sample B2 at selected tilt angles θ from 0° to 120° ($T = 2$ K). (c, d) Field positions of the oscillating extrema for samples A1 and B2, respectively. Dashed lines show the $B_0/\cos\theta$ fit for sample A1 and tentative $B_0/\cos(\theta - 30°)$ curves for sample B2. (e) The ρ_{xx} curves as a function of B_v at 2 K and at a lower field for sample A1.

an increase at high temperatures followed by a decrease and another increase at lower temperatures. The increase at low temperatures of n-type samples is more obvious than that of p-type samples. The maximum of $\rho_{xx}(T)$ can be explained by the thermal activation model, while the minimum of resistivity at lower temperatures is possibly related to a charge-density-wave transition as reported for β-Bi_4I_4 [22,24]. Here we choose A1 and B2 as the representatives of n-type and p-type samples, respectively, for further analysis. Using a single-band model, we estimate that the carrier density n_{3D}^{Hall} and Hall mobility μ^{Hall} of A1 are about 2.59×10^{18} cm^{-3} and 954 cm^2/V s and those of B2 are 1.66×10^{18} cm^{-3} and 3507 cm^2/V s.

Figure 2(a) shows the magnetoresistance ($MR = [R_{xx}(H) - R_{xx}(0)]/R_{xx}(0)$) at 2 K for A1 and B2 with $\theta = 0°$ and 30°, respectively, values which correspond to the maximal oscillation period as displayed below. Here θ is defined as the angle between the normal direction of the sample's top surface and the magnetic field, as shown schematically in the inset in Fig. 3(a). At low magnetic fields, the MR of both samples shows a cusplike feature, which fades away with increasing temperature (see Supplemental Fig. S2 [23]) and is attributed to the WAL effect [25–27]. Generally, the WAL effect occurs in a system with a π berry phase or strong spin-orbital coupling [25,28]. Considering that α-Bi_4I_4 is a trivial insulator, the WAL behavior comes from the strong spin-orbit coupling. Above 2 T, SdH oscillations are obviously observed. To extract the SdH oscillations, we determine the background curves as the average of the MR envelope curves as shown in Fig. 2(b) [8]. The robustness of the results to the background extraction has been discussed by trying different background curves, as reported in the Supplemental Material [23]. The extracted $\Delta\rho_{xx}$ is periodic in the inverse magnetic field $1/B$ [Fig. 2(c)], which is a typical characteristic of single-frequency SdH oscillations. The inset in Fig. 2(c) shows that oscillations decay with the temperature, another feature of SdH oscillations. Figure 2(d) displays the MR background curves for A1 and B2 at $\theta = 0°$ and 30°, respectively. Interestingly, a large negative MR is found in sample A1 at high fields, up to −33% at 14 T. For a nonmagnetic system, the large negative MR in the transverse configuration (current $j \perp B$) is unusual. The weak localization effect is a possible explanation for the transverse negative MR [29,30]. However, it should not be applicable here at such high magnetic fields, where the system is out of the quantum diffusive regime [29,31]. Recently, it has been proposed that charge puddles caused by strong fluctuations of the Coulomb potential could be responsible for the gigantic negative MR with both the longitudinal and the transverse configurations in disordered narrow-gap systems [32]. The theory provides a possible way to explain the large negative MR, which needs to be verified by further study.

To analyze the origin of the SdH oscillations, the resistance derivative dR_{xx}/dB as a function of $1/B$ at different angles was investigated. For sample A1, the oscillating period decreases with increasing tilt angles, and the strong quantum oscillations at $\theta = 0°$ fade out gradually and are absolutely absent at $75° < \theta < 105°$ (Supplemental Fig. S3)

[23]. When plotted in $1/B_v = 1/(B\cos\theta)$, the dR_{xx}/dB of A1 has the same oscillating periods at tilt angles $\theta < 60^\circ$, with all maxima and minima lining up at the same positions [see Fig. 3(a)]. The oscillations depending solely on B_v reveal a 2D nature [6], which is also confirmed in Fig. 3(c), where the angle dependence of extrema for sample A1 scales as $1/\cos\theta$. On the other hand, the oscillations in B2 survive at all measured tilt angles [Fig. 3(b)], and the peak positions deviate from $1/\cos(\theta - \theta_0)$ for any θ_0 with $(\theta - \theta_0) > 50^\circ$ [Fig. 3(d)]. These indicate that the oscillations in sample B2 are from the contributions of a 3D FS. As shown in Fig. 3(d), despite the deviation from a 2D nature, oscillations in sample B2 show strong anisotropy, and the angular dependence indicates a likely ellipsoid FS in B2 [10]. In addition, when plotted as a function of the normal field component (B_v), the WAL curves measured at different tilt angles merge, as shown in Fig. 3(e). The angular-dependent WAL effect in sample A1 further confirms the 2D electronic behavior [27]. In addition, for sample A1, the trend of negative MR survives at all measured tilt angles, indicating a bulk effect.

According to the standard Lifshitz-Kosevich (LK) theory, the resistivity oscillates as $\Delta\rho_{xx} \sim \frac{\lambda}{\sinh\lambda} e^{-\lambda_D} \cos[2\pi(F/B + 1/2 - \gamma + \delta)]$ [33,34], where F is the oscillating frequency, $\lambda = 2\pi^2 k_B T/\hbar\omega_c$, $\lambda_D = 2\pi^2 k_B T_D/\hbar\omega_c$, with T_D the Dingle temperature and the cyclotron frequency $\omega_c = eB/m_c$ (m_c is the cyclotron effective mass). γ is related to the Berry phase β by $\beta = 2\pi\gamma$, and δ is a phase shift determined by the dimensionality with the value of $\delta = \pm\frac{1}{8}$ or 0 for a 3D or 2D system. It is well known that, in metals, SdH oscillations correspond to successive emptying of Landau levels (LLs) with increasing magnetic field. The LL index n is related to the cross section S_F of the FS: $n = \frac{\hbar S_F}{2\pi e}\frac{1}{B} - \gamma + \delta$ by the Onsager relation $F = \frac{\hbar S_F}{2\pi e}$, where the integer n denotes the nth LL. Figures 4(a) and 4(b) display the LL fan diagrams indexed by the above relation for samples A1 and B2. Considering the bulk transport with a considerable carrier density, the peak positions in $\Delta\rho_{xx}$ are assigned to the integer Landau index, and the dip positions in $\Delta\rho_{xx}$ are assigned to the half-integer Landau index [8,35]. It is shown that the inverse fields $1/B$ fall on a straight line versus the index n, and extrapolation at the extreme field limit ($1/B \to 0$) gives $(-\gamma + \delta) \sim 0.17$ and 0.06 for samples A1 and B2 with $\delta = 0$ and $\pm\frac{1}{8}$, respectively. The intercepts obtained come significantly closer to 0 instead of $\pm\frac{1}{2}$, which indicates that the oscillations originate from the topological trivial state. It is noteworthy that an LL index of 1 appears below 14 T, suggesting that the system approaches the quantum limit. Furthermore, the slope of the fan diagram yields $S_F^{\rm SdH} = 1.02 \times 10^{-3}$ Å^{-2} with Fermi wave vector $k_F^{\rm SdH} = 1.81 \times 10^{-2}$ Å^{-1} for sample A1, and the smallest $S_F^{\rm SdH}$ of sample B2 is 0.97×10^{-3} Å^{-2} with $k_F^{\rm SdH} = 1.76 \times 10^{-2}$ Å^{-1}. In addition, the largest cross section of B2 is estimated at about 0.0036 Å^{-2}, and the longest k_F is roughly estimated at about 0.065 Å^{-1} with an ellipsoid FS approximation [10].

To extract more information from the quantum oscillations, we further analyze the SdH amplitude's variation with the temperature. According to the LK theory, the temperature-dependent SdH amplitudes $\Delta\rho_{xx} \sim \frac{2\pi^2 k_B T/\hbar\omega_c}{\sinh(2\pi^2 k_B T/\hbar\omega_c)}$ can be used to determine the cyclotron effective mass m_c. As shown

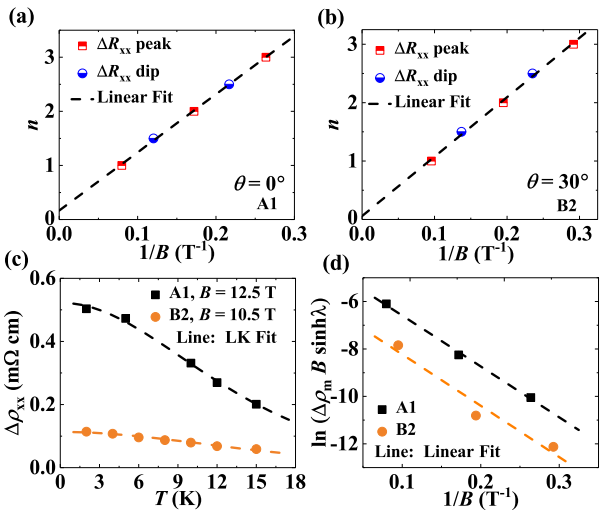

FIG. 4. LL fan diagram for the oscillations in R_{xx} for (a) sample A1 at $\theta = 0^\circ$ and (b) sample B2 at $\theta = 30^\circ$. The peaks of $\Delta\rho_{xx}$ correspond to the integer n, and the dips correspond to the half-integer $n + \frac{1}{2}$. (c) Temperature dependence of the SdH amplitude for A1 at $\theta = 0^\circ$ and B2 at $\theta = 30^\circ$; dashed lines represent the fitting curves by the Lifshitz-Kosevich theory. (d) Dingle plot for the oscillations in ρ_{xx} measured at 2 K for A1 at $\theta = 0^\circ$ and B2 at $\theta = 30^\circ$ and the linear fitting.

in Fig. 4(c), the m_c is estimated at about 0.15 m_e for sample A1 and 0.11 m_e for sample B2, where m_e is the free electron mass. The Fermi velocity v_F can be calculated with simple calculations: $v_F^{\rm SdH} = 1.41 \times 10^5$ m/s for sample A1 and 1.92×10^5 m/s for sample B2, as listed in Table I.

At a fixed temperature T, $\Delta\rho_{xx}$ decays by the factor $\frac{\lambda}{\sinh\lambda} e^{-\lambda_D}$, where $\lambda_D = \frac{2\pi^2 k_B m_c T_D}{e\hbar B} = \frac{\pi m_c}{e\tau B}$, which is related to the Dingle temperature T_D and the carrier scattering time τ. Figure 4(d) is the Dingle plot at 2 K for samples A1 and

TABLE I. Parameters in samples A1 and B2 determined by the SdH oscillations, Hall effect, and DFT calculations.

	Sample A1	Sample B2
From SdH oscillations		
$S_F^{\rm SdH}$ (10^{-3} Å^{-2})	1.02	0.97
$k_F^{\rm SdH}$ (10^{-2} Å^{-1})	1.81	1.76
$m_c^{\rm SdH}$ (m_e)	0.15	0.11
$v_F^{\rm SdH}$ (10^5 m/s)	1.41	1.92
$T_D^{\rm SdH}$ (K)	9.8	13.9
$\tau^{\rm SdH}$ (10^{-13} s)	1.24	0.88
$\ell^{\rm SdH}$ (nm)	17.4	16.8
$\mu^{\rm SdH}$ (cm^2/V s)	1464	1451
$n_{\rm 3D}^{\rm SdH}$ (10^{18} cm^{-3})	2.62	1.36
From the Hall effect		
$n_{\rm 3D}^{\rm Hall}$ (10^{18} cm^{-3})	2.59	1.66
$\mu^{\rm Hall}$ (cm^2/V s)	954	3507
$\tau^{\rm Hall}$ (10^{-13} s)	4.44	15.06
From DFT calculations		
$n_{\rm 3D}^{\rm DFT}$ (10^{18} cm^{-3})	2.64	1.42

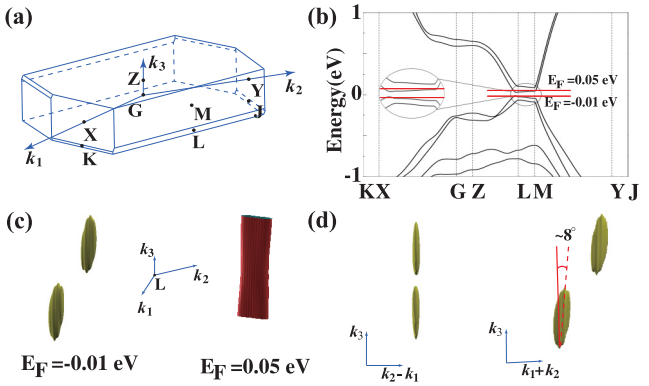

FIG. 5. (a) Bulk Brillouin zone of α-Bi_4I_4. (b) Band structure of α-Bi_4I_4. The Fermi levels $E_F = 0.05$ and -0.01 eV for conduction and valence bands are represented by red lines. (c) Fermi surfaces (FSs) drawn with $E_F = -0.01$ and 0.05 eV relative to the intrinsic Fermi level. The reciprocal lattice vectors correspond to the primitive cell used in first-principles calculations. The relationship between primitive and conventional cells is reported in the Supplemental Material [23]. (d) Side views of the FS with $E_F = -0.01$ eV looking in the direction of $k_1 + k_2$ and $k_1 - k_2$, respectively. The direction of $k_1 - k_2$ is parallel to the b axis in the conventional unit cell.

B2, and dashed lines represent the linear fit. The slopes yield T_D^{SdH} of 9.8 and 13.9 K, which give $\tau^{\mathrm{SdH}} = 1.24 \times 10^{-13}$ and 0.88×10^{-13} s, respectively. Consequently, the lower bound of the electron mean-free path $\ell^{\mathrm{SdH}} = v_F\tau$ is about 17.4 nm for A1 and 16.8 nm for B2, and the low-limit mobility μ^{SdH} is estimated to be 1464 $\mathrm{cm}^2/\mathrm{V\,s}$ for A1 and 1451 $\mathrm{cm}^2/\mathrm{V\,s}$ for B2.

IV. DENSITY FUNCTIONAL THEORY (DFT) CALCULATIONS AND DISCUSSION

To further investigate the origin of the different magnetotransport behaviors between n-type and p-type samples, we performed first-principles calculations based on the DFT. The bulk band structure of α-Bi_4I_4 is shown in Fig. 5(b). According to the FS cross sections obtained by the SdH oscillations, the Fermi levels are determined at about 0.05 and -0.01 eV for the n-type sample A1 and p-type sample B2, respectively, as illustrated in the inset in Fig. 5(b). The FS of A1 is tubular, with a long axis parallel to the k_3 axis (perpendicular to the ab plane of the crystal), as shown in the right panel in Fig. 5(c). Meanwhile, the left panel in Fig. 5(c) indicates that the FS of B2 is 3D, consisting of two ellipsoid FSs connected by time-reversal symmetry. Figure 5(d) shows side views of the two ellipsoid FSs along the direction of $k_1 + k_2$ and $k_1 - k_2$. The 2D FS for A1 and 3D FS for B2 explain the corresponding SdH oscillation behaviors.

The carrier densities calculated from the size of the FS are about $n_{3\mathrm{D}}^{\mathrm{DFT}} = 2.64 \times 10^{18}$ cm^{-3} and $n_{3\mathrm{D}}^{\mathrm{DFT}} = 1.42 \times 10^{18}$ cm^{-3} for samples A1 and B2, respectively. With the cross sections of FSs obtained from SdH oscillations, the bulk carrier densities $n_{3\mathrm{D}}^{\mathrm{SdH}}$ can also be estimated as 2.62×10^{18} cm^{-3} for A1 and 1.36×10^{18} cm^{-3} for B2, with two Fermi pockets considered for B2 [10]. The calculated $n_{3\mathrm{D}}^{\mathrm{DFT}}$ and $n_{3\mathrm{D}}^{\mathrm{SdH}}$ for A1 and B2 agree with the values obtained from the Hall resistivity. The values of the mean scattering time τ^{Hall} have been roughly estimated with the Hall mobility and effective mass m^* calculated from the band structure around band edges, which are about 4.44×10^{-13} and 15.06×10^{-13} s for samples A1 and B2, respectively. The scattering time τ^{Hall} is larger than τ^{SdH} for both samples, as τ obtained from SdH oscillations is shortened by more scattering processes [7,36]. All these parameters are listed in Table I. For the 3D SdH oscillations in B2, the minimum frequency takes place at about $\theta = 30^\circ$ between the magnetic field and the k_3 axis. However, the normal direction of the minimum cross section in Fig. 5(d) is nearly 8° away from the normal direction of the ab surface. The disagreement between the electronic-structure calculations and the experimental results requires further research.

Due to the similar crystal structure, it is instructive to compare the bulk electronic structure of α-Bi_4I_4 with the TI β-Bi_4I_4. We calculated the bulk band structure of β-Bi_4I_4 and obtained the FSs with E_F located at different positions. It is surprising that in a relatively wide range of E_F values, the FSs of the conduction band and valance band are nearly 2D and 3D, respectively. Two typical bulk FSs of β-Bi_4I_4 are shown in the Supplemental Material [23]. The 2D transport of bulk electrons observed in n-type α-Bi_4I_4 samples suggests that it should be cautious to identify the possible TSS in future transport experiments on the TI β-Bi_4I_4, which has a bulk electronic structure similar to that of the α phase.

V. CONCLUSION

In summary, the transport properties of α-Bi_4I_4 with a quasi-one-dimensional structure have been studied with high-quality single crystals. Two kinds of samples with different carrier types are investigated. Two-dimensional SdH oscillations and the WAL effect of the magnetoresistance are observed in n-type samples, while oscillations in p-type samples are 3D with strong anisotropy. The analysis of the LL fan diagrams yields a Berry phase close to 0 for both kinds of samples, suggesting topological trivial states. The large SdH oscillations, achieving an LL index of 1 below 14 T, provide the opportunity to investigate the novel properties in the quantum limit under relatively modest magnetic fields. First-principles calculations show that the FSs of n-type samples are 2D, while the FSs of p-type samples are 3D. In addition, a large negative MR in the transverse configuration is observed in sample A1, which is peculiar and deserves further investigation. These results make α-Bi_4I_4 an important platform for investigation of these novel properties and a valuable reference for understanding the topological surface properties of β-Bi_4I_4 in the future.

ACKNOWLEDGMENTS

The authors thank Yongqing Li, Cheng-Cheng Liu, Haiwen Liu, Hai-Zhou Lu, Shuang Jia, and Zhi-An Ren for valuable discussions and selfless help. This work was financially supported primarily by the National Nature Science Foundation of China (Grant No. 11734003) and the National Key

Research and Development Program of China (Grant No. 2016YFA0300604).

D.-Y.C. and D.-S.M. contributed equally to the present work.

[1] M. Z. Hasan and C. L. Kane, Rev. Mod. Phys. **82**, 3045 (2010).
[2] J. E. Moore, Nature **464**, 194 (2010).
[3] X.-L. Qi and S.-C. Zhang, Rev. Mod. Phys. **83**, 1057 (2011).
[4] D. Culcer, Physica E **44**, 860 (2012).
[5] J. G. Analytis, R. D. McDonald, S. C. Riggs, J. H. Chu, G. S. Boebinger, and I. R. Fisher, Nat. Phys. **6**, 960 (2010).
[6] D.-X. Qu, Y. S. Hor, J. Xiong, R. J. Cava, and N. P. Ong, Science **329**, 821 (2010).
[7] Z. Ren, A. A. Taskin, S. Sasaki, K. Segawa, and Y. Ando, Phys. Rev. B **82**, 241306(R) (2010).
[8] J. Xiong, Y. Luo, Y. H. Khoo, S. Jia, R. J. Cava, and N. P. Ong, Phys. Rev. B **86**, 045314 (2012).
[9] E. K. de Vries, S. Pezzini, M. J. Meijer, N. Koirala, M. Salehi, J. Moon, S. Oh, S. Wiedmann, and T. Banerjee, Phys. Rev. B **96**, 045433 (2017).
[10] F. Qu, C. Zhang, R.-R. Du, and L. Lu, J. Low Temp. Phys. **170**, 397 (2013).
[11] M. Bianchi, D. Guan, S. Bao, J. Mi, B. B. Iversen, P. D. C. King, and P. Hofmann, Nat. Commun. **1**, 128 (2010).
[12] H. M. Benia, C. Lin, K. Kern, and C. R. Ast, Phys. Rev. Lett. **107**, 177602 (2011).
[13] M. S. Bahramy, P. D. C. King, A. de la Torre, J. Chang, M. Shi, L. Patthey, G. Balakrishnan, P. Hofmann, R. Arita, N. Nagaosa, and F. Baumberger, Nat. Commun. **3**, 1159 (2012).
[14] J. G. Analytis, J.-H. Chu, Y. Chen, F. Corredor, R. D. McDonald, Z. X. Shen, and I. R. Fisher, Phys. Rev. B **81**, 205407 (2010).
[15] B. Skinner, T. Chen, and B. I. Shklovskii, Phys. Rev. Lett. **109**, 176801 (2012).
[16] J.-J. Zhou, W. Feng, C.-C. Liu, S. Guan, and Y. Yao, Nano Lett. **14**, 4767 (2014).
[17] J.-J. Zhou, W. Feng, G.-B. Liu, and Y. Yao, New J. Phys. **17**, 015004 (2015).
[18] G. Autès, A. Isaeva, L. Moreschini, J. C. Johannsen, A. Pisoni, R. Mori, W. Zhang, T. G. Filatova, A. N. Kuznetsov, L. Forró, W. Van den Broek, Y. Kim, K. S. Kim, A. Lanzara, J. D. Denlinger, E. Rotenberg, A. Bostwick, M. Grioni, and O. V. Yazyev, Nat. Mater. **15**, 154 (2016).
[19] C.-C. Liu, J.-J. Zhou, Y. Yao, and F. Zhang, Phys. Rev. Lett. **116**, 066801 (2016).
[20] F. Tang, H. C. Po, A. Vishwanath, and X. Wan, arXiv:1805.07314.
[21] H. G. v. Schnering, H. v. Benda, and C. Kalveram, Z. Anorg. Allg. Chem. **438**, 37 (1978).
[22] T. G. Filatova, P. V. Gurin, L. Kloo, V. A. Kulbachinskii, A. N. Kuznetsov, V. G. Kytin, M. Lindsjo, and B. A. Popovkin, J. Solid State Chem. **180**, 1103 (2007).
[23] See Supplemental Material at http://link.aps.org/supplemental/10.1103/PhysRevMaterials.2.114408 for further details on sample characterization, magnetotransport properties, and first-principles calculations.
[24] A. Pisoni, R. Gaál, A. Zeugner, V. Falkowski, A. Isaeva, H. Huppertz, G. Autès, O. V. Yazyev, and L. Forró, Phys. Rev. B **95**, 235149 (2017).
[25] Y. Ando, J. Phys. Soc. Jpn. **82**, 102001 (2013).
[26] Y. Nakajima, P. Syers, X. Wang, R. Wang, and J. Paglione, Nat. Phys. **12**, 213 (2016).
[27] K. Shrestha, D. Graf, V. Marinova, B. Lorenz, and C. W. Chu, J. Appl. Phys. **122**, 145901 (2017).
[28] S. Hikami, A. I. Larkin, and Y. Nagaoka, Prog. Theor. Phys. **63**, 707 (1980).
[29] P. A. Lee and T. V. Ramakrishnan, Rev. Mod. Phys. **57**, 287 (1985).
[30] E. P. Amaladass, T. R. Devidas, S. Sharma, and A. Mani, J. Phys.: Condens. Matter **29**, 175602 (2017).
[31] H.-Z. Lu and S.-Q. Shen, Chin. Phys. B **25**, 117202 (2016).
[32] O. Breunig, Z. Wang, A. A. Taskin, J. Lux, A. Rosch, and Y. Ando, Nat. Commun. **8**, 15545 (2017).
[33] I. M. Lifshitz and A. M. Kosevich, Sov. Phys. JETP **2**, 636 (1956).
[34] X. Huang, L. Zhao, Y. Long, P. Wang, D. Chen, Z. Yang, H. Liang, M. Xue, H. Weng, Z. Fang, X. Dai, and G. Chen, Phys. Rev. X **5**, 031023 (2015).
[35] J. Xiong, Y. Khoo, S. Jia, R. J. Cava, and N. P. Ong, Phys. Rev. B **88**, 035128 (2013).
[36] A. Narayanan, M. D. Watson, S. F. Blake, N. Bruyant, L. Drigo, Y. L. Chen, D. Prabhakaran, B. Yan, C. Felser, T. Kong, P. C. Canfield, and A. I. Coldea, Phys. Rev. Lett. **114**, 117201 (2015).